Satellite-based estimates of nitrogen oxide and methane emissions from gas flaring and oil production activities in Sakha Republic, Russia

Ialongo, Iolanda

2021

Ialongo , I , Stepanova , N , Hakkarainen , J , Virta , H & Gritsenko , D 2021 , ' Satellite-based estimates of nitrogen oxide and methane emissions from gas flaring and oil production activities in Sakha Republic, Russia ' , Atmospheric Environment. X , vol. 11 , 100114 . https://doi.org/10.1016/j.aeaoa.2021.100114

http://hdl.handle.net/10138/339480
https://doi.org/10.1016/j.aeaoa.2021.100114

ATMOSPHERIC ENVIRONMENT: X 11 (2021) 100114

Contents lists available at ScienceDirect

Atmospheric Environment: X

journal homepage: www.journals.elsevier.com/atmospheric-environment-x

Satellite-based estimates of nitrogen oxide and methane emissions from gas flaring and oil production activities in Sakha Republic, Russia

Iolanda Ialongo [a,*], Nadezhda Stepanova [b,c], Janne Hakkarainen [a], Henrik Virta [a], Daria Gritsenko [c]

[a] Space and Earth Observation Centre, Finnish Meteorological Institute, Helsinki, Finland
[b] Arctic Scientific Center of Sakha Academy of Sciences, Yakutsk, Russia
[c] Russian and Eurasian Studies (Aleksanteri Institute), University of Helsinki, Finland

ARTICLE INFO

Keywords:
Gas flaring
Oil extraction
TROPOMI
Nitrogen dioxide
Methane
Emissions
VIIRS fire

ABSTRACT

Crude oil production activities and associated petroleum gas (APG) flaring are responsible for significant air polluting and greenhouse gas (GHG) emissions and have negative effects on the environment and climate. In Russia, one of the world's major oil producers, APG flaring remains a routine practice despite regulatory policies. We present the first analysis of nitrogen oxide and methane emissions over Tas-Yuryakh and Talakan oil fields in Sakha Republic (Eastern Siberia, Russia) using multi-satellite observations.

Satellite-based TROPOMI (TROPOspheric Monitoring Instrument) nitrogen dioxide (NO_2) mean fields show local NO_2 enhancements corresponding to the locations of gas flares detected from Sentinel 2 imagery and VIIRS (Visible Infrared Imaging Radiometer Suite) fire data. We derive the annual nitrogen oxide ($NO_x = NO_2$+NO) emissions from TROPOMI NO_2 observations using an exponentially-modified Gaussian model. We obtain NO_x emissions up to 1.34 mol/s (in 2019) in Tas-Yuryakh, where persistent production APG flaring is detected, and about 0.6 mol/s in Talakan, where oil production is three times larger than in Tas-Yuryakh but gas flaring is employed only occasionally. In 2019 we observe a new flaring site in Tas-Yuryakh from the NO_2 mean fields, corresponding to an increase in the environmental fees paid by the companies to the local budgets. Assuming that all NO_x emissions are associated with APG flaring, the volume of gas flared for 2019 is estimated at 1.25 ± 0.48 billion cubic metres (bcm) in Tas-Yuryakh and 0.5 ± 0.2 bcm in Talakan.

Furthermore, we find a clear methane (CH_4) anomaly of about 30 ppb from the TROPOMI XCH_4 mean fields near Talakan oil field. We estimate CH_4 emissions of about 28–63 tons/h from individual TROPOMI XCH_4 plumes using the cross-sectional flux method.

The estimated satellite-based NO_x and CH_4 emissions are higher than the inventories, which are expected to underestimate the contribution from the oil and gas industry and are generally available with several years of delay. TROPOMI NO_2 and CH_4 observations demonstrate their capability in identifying emission sources from space with unprecedented detail. The results show how satellite observations can support environmental authorities in monitoring the emissions from the oil and gas industry and the commitment of oil companies in reducing APG flaring.

1. Introduction

Associated petroleum gas (APG) flaring is a diffuse practice in the oil industry that can have significant effects on the environment and climate, due to the associated air polluting and greenhouse gas (GHG) emissions. As the oil is extracted, the APG, present in solution with the crude oil, is released. Part of this gas can be captured during the extraction process to be used as fuel, but often it is released to flare during the oil extraction, production or processing phases. Gas flaring from oil extraction emits several air pollutants, including nitrogen oxides ($NO_x = NO + NO_2$) and methane (CH_4) among other components. Methane is also emitted through leakages or venting during oil production.

Nitrogen dioxide (NO_2) is a short-lived gas (lifetime of a few hours)

* Corresponding author.
E-mail address: iolanda.ialongo@fmi.fi (I. Ialongo).

https://doi.org/10.1016/j.aeaoa.2021.100114
Received 12 March 2021; Received in revised form 20 May 2021; Accepted 23 May 2021
Available online 1 June 2021

mainly generated by combustion processes from anthropogenic sources including energy, transportation and other industrial sectors. NO_2 plays an important role in tropospheric chemistry, participating in ozone and aerosol production, and it is harmful for human health when present in high concentrations at the surface. On the other hand, CH_4 is the second most important man-made greenhouse gas, after carbon dioxide (CO_2). Despite methane's shorter residence time (about 9 years), CH_4 has a 28 times higher warming potential (in 100 years) than CO_2 (IPCC, 2014). Oil and gas industry is among the main sources of anthropogenic methane emissions.

The emission estimates of air pollutants over oil fields and in particular those related to APG flaring are considered to be uncertain and incomplete (Li et al., 2016; Elvidge et al., 2016). Due to their global coverage, satellite-based observations are suitable for monitoring air polluting emissions from different sources, especially in absence of other monitoring systems. Since April 2018, TROPOMI (TROPOspheric Monitoring Instrument), the only payload on-board the Sentinel-5 Precursor (S5P) satellite of the European Space Agency (ESA), has been providing NO_2 tropospheric column retrievals with the best available spatial resolution (3.5×7 km^2 at the beginning of the mission and 3.5×5.5 km^2 since 6 August 2019) and signal-to-noise ratio (Veefkind et al., 2012). In addition to NO_2, TROPOMI provides observations of methane from the infrared channel with near-nadir resolution of 7×7 km^2 (and 7×5.5 km^2 since 6 August 2019).

Several data-driven methods have been applied to calculate air polluting emissions from point sources based on satellite observations from TROPOMI and other previous instruments (Beirle et al., 2011; Fioletov et al., 2015; Varon et al., 2018; Goldberg et al., 2019). In particular, satellite-based data have been used for monitoring the emissions from the oil and gas industrial sector (e.g., McLinden et al., 2014; Varon et al., 2019; Dix et al., 2020; van der A et al., 2020; de Gouw et al., 2020; Zhang et al., 2020; Schneising et al., 2020; Crosman, 2021), including studies focusing on the effects of gas flaring (Li et al., 2016; Zhang et al., 2019).

In addition, gas flaring has been studied using VIIRS (Visible Infrared Imaging Radiometer Suite) fire products (Schroeder et al., 2014). For example, Elvidge et al. (2016) compiled a global survey of volume of associated gas based on the VIIRS nightfire product, which is particularly suited to monitor small fires as the gas flares. Many of these studies analyse oil and gas fields in the United States, with some exceptions focusing on areas in Turkmenistan, Algeria and off-shore sites in Mexico, as well as large scale analysis in the Arctic. van der A et al. (2020) analysed the NO_2 emissions from natural gas extraction and transport along the West Siberian pipeline.

Russia is one of the world's largest oil producers and its extractive industry is responsible for the largest volume of gas flared associated with oil production (Elvidge et al., 2016). In 2018 the volume of APG flaring in the country was about 58% larger than the 1990 level (Russian Federation, 2020). Despite the introduction of regulations by the Russian government in 2012 to reduce APG flaring, the goal for the gas utilization rate of 95% was not reached at national level, partly due to the development of new oil deposits in Eastern Siberia (Vorobev and Shchesnyak, 2019). The policy is designed in such a way, that for oil companies it appears less expensive to pay the fees for the extra gas flaring rather than investing in APG processing facilities (Rustamov and Bryukhova, 2019).

In this study, we present the first analysis of the NO_x and CH_4 emissions over the Tas-Yuryakh and Talakan oil fields in Sakha Republic (Eastern Siberia, Russia) by using multiple satellite observations, with particular focus on the impact of the APG flaring. We apply a multi-satellite approach to detect the location and frequency of the flares and the corresponding emissions, by using TROPOMI NO_2 and CH_4 products, VIIRS active fire data and Sentinel 2 false color imagery. Finally, we evaluate how the different companies operating at the two oil fields manage the disposal of the APG.

2. Data and methodology

2.1. Tas-Yuryakh and Talakan oil fields

The largest part of crude oil production in Sakha Republic takes place in the south-western part of the region at two locations: Tas-Yuryakh in the Mirninsky district (operated by Rosneft and RNG companies) and Talakan in the Lensky district (operated by Surgutneftegas). Fig. 1 shows the location of the study area and the annual TROPOMI NO_2 mean fields for 2019 over south-west Sakha Republic. In both areas the oil produced feeds into the Eastern Siberia–Pacific Ocean (ESPO) pipeline, designed for exporting Russian crude oil to the Asia-Pacific markets. Tables 1 and 2 include the crude oil production in 2018–2019 in Tas-Yuryakh and Talakan, respectively.

In the Mirninsky district most of the oil production (3944 Kton in 2019) occurs in Tas-Yuryakh at the Central block and Kurungky area of the Srednebotuobinskoye deposit developed by the Rosneft affiliated JSC Taas Yuryakh Neftegazodobycha (#1 in Fig.2, upper panels). This is the third largest asset of Rosneft in Eastern Siberia, accounting for 99.3% and 89.2% of the total oil extracted in the Mirninsky district in 2018 and 2019, respectively. In 2019, the LC RNG company started extraction activities in the Eastern block of the same deposit (located 30 km north-east from the Central block) with 853 Kton of crude oil extracted (#2 in Fig.2, upper panels).

In the Lensky district, Surgutneftegas company has eight licenses to operate, including the main oil extracting facilities at the Talakan oil and gas field. The oil production in Talakan started in 2012 and it amounted to over 9000 Kton/year in 2019 (Table 2), which is about 67.4% of the total volume for oil extraction industry in Sakha Republic and about three times the oil production in Tas-Yuryakh. Surgutneftegas declares to utilize up to 99% of the accompanying gas and in Sakha Republic it reached 98.23% in 2019, according to the State Annual Report on the Environment in the Sakha Republic (Yakutia) in 2019.

According to the Russian Federation (RF) regulation, companies can flare up to 5% of APG in the oil extraction process. For the volume exceeding the allowed limits, the companies need to pay negative environmental impact fees with an additional factor of 25 applied to the rates of the basic fees. These fees are calculated by the emitting company based on measurements of the different polluting components and on the rates of charges established by the national authorities. The Federal Service for Supervision of Natural Resources - Rosprirodnadzor - is the responsible authority for controlling over the correct calculation, completeness and timeliness of payment for the whole Russian Federation.

According to the RF Budgetary Code, the negative environmental impact fee is divided as follows: 55% (60% since 2020) is directed to the budget of the municipal district where the emission has taken place, 5% to the federal budget (0% since 2020), and the rest (40%) to the regional budget. Tables 1 and 2 show the sums paid to the budget of Mirninsky and Lensky municipal districts (respectively) for the APG flaring. The fees paid to the Mirninsky district are significantly larger than those paid to the Lensky district, in 2019 amounting to ca. 31 million rubles and ca. 15 thousand rubles, respectively.[1]

2.2. TROPOMI NO_2 product and emission estimation method

We use satellite-based NO_2 tropospheric columns from TROPOMI (TROPOspheric Monitoring Instrument) to derive the NO_x emissions over the Tas-Yuryakh and Talakan oil fields. TROPOMI is a passive-sensing hyperspectral nadir-viewing imager aboard the Copernicus Sentinel-5 Precursor (S5P) satellite, launched on 13 October 2017. S5P is a near-polar sun-synchronous orbiting satellite with an overpass local

[1] All the socio-economic data reported in this work are available as reported in Sect. 5.

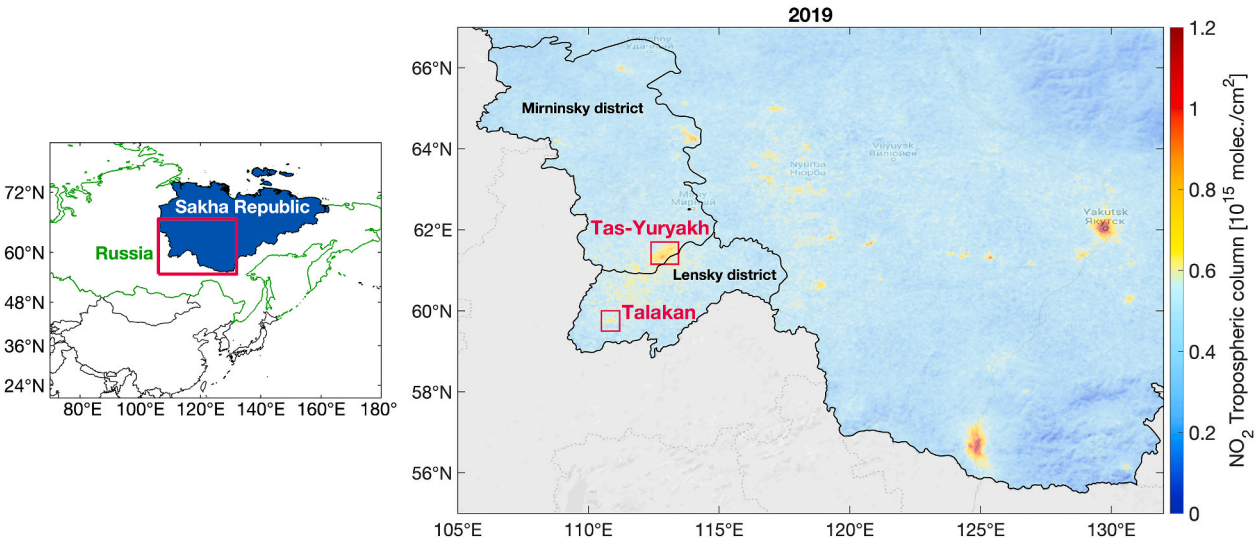

Fig. 1. Left panel: Map of Sakha Republic, Russia (blue area). The Russian borders are shown in green. The pink rectangle indicates the area covered by the map in the right panel. Right panel: Annual TROPOMI NO_2 average map for 2019 over south-west Sakha Republic. The data outside of Sakha Republic are not shown. The location of Tas-Yuryakh (Mirninsky district) and Talakan (Lensky district) oil fields is shown as pink rectangles. In addition to the oil fields, NO_2 enhancements are visible for example over the city of Yakutsk (the capital of Sakha Republic) and in the south over Neryungri coal-mining complex.

Table 1
Summary of the results in Tas-Yuryakh.

Year	Fire counts		Daytime FRP (MW)	NO_x emission (mol/s)	Volume of gas flared (bcm)		Oil production (Ktons)		Flaring fees (10^6 rubles)
	Day	Night							
	#1/#2[⋆]	#1/#2	#1/#2		TROPOMI	VIIRS[Ш]	#1	#2	
2018	558/5	1527/134	14.5/3.7	0.61 ± 0.24[†]	0.57 ± 0.22[†]	0.40 ± 0.04	2884	–	19.387
2019	561/452	1688/1128	19.8/15.1	1.34 ± 0.46	1.25 ± 0.48	1.14 ± 0.11	3944.7	853.85	31.3688
2020	784/416[⋆]	1960/994[⋆]	24.9/12.6[⋆]	1.02 ± 0.39	0.95 ± 0.37	–	–	–	–

[†]The NOx emissions and the corresponding volume of gas flared calculated for year 2018 include only TROPOMI data from 15 April to the end of the year.
[⋆]The 2020 total fire counts and mean FRP values include near real time VIIRS active fire data during the period of 1 June 2020–31 December 2020 and standard product before 1 June 2020.
[‡]Number of the facility.
[Ш]From the survey by Elvidge et al. (2016).

Table 2
Summary of the results in Talakan.

Year	Fire counts		Daytime FRP (MW)	NO_x emission (mol/s)	Volume of gas flared (bcm)		Oil production (Ktons)	Flaring fees (10^3 rubles)
	Day	Night			TROPOMI	VIIRS[Ш]		
2018	45	62	6.3	0.61 ± 0.29[†]	0.57 ± 0.27[†]	0.025 ± 0.003	9130.0	59
2019	53	88	10.7	0.57 ± 0.22	0.52 ± 0.22	0.023 ± 0.002	9341.85	14.7
2020	76[⋆]	100[⋆]	8.7[⋆]	0.60 ± 0.24	0.56 ± 0.23	–	–	–

[†]The NO_x emissions and the corresponding volume of gas flared calculated for year 2018 include only TROPOMI data from 15 April to the end of the year.
[⋆]The 2020 total fire counts and mean FRP values include near real time VIIRS active fire data during the period of 1 June 2020–31 December 2020 and standard product before 1 June 2020.
[Ш] from the survey by Elvidge et al. (2016).

time of 13:30 (Veefkind et al., 2012). TROPOMI measures in the ultraviolet–visible (UV-VIS), near-infrared (NIR) and short-wavelength infrared (SWIR) spectral bands. The NO_2 tropospheric columns are derived from TROPOMI's UV–VIS spectrometer backscattered solar radiation measurements (van Geffen et al., 2019). The 2600 km -wide swath is divided into 450 individual measurement pixels, with a near-nadir resolution of 3.5 × 7 km^2. Since 6 August 2019 the spatial resolution for the UV-VIS channel has been further improved to 3.5 × 5.5 km^2. In the analysis we use the TROPOMI NO_2 product versions 1.2 (1 April 2018–20 March 2019) and 1.3 (20 March 2019–30 November 2020). The TROPOMI NO_2 products are routinely validated by the S5P-MPC-VDAF (S5P – Mission Performance Center – Validation Data Analysis Facility) using ground-based observations. For example, Griffin et al. (2019) and Ialongo et al. (2020) found high correlations between TROPOMI NO_2 retrievals and ground-based observations over the Canadian oil sands and at a high-latitude urban site in Helsinki, Finland, respectively.

In order to map the NO_2 distribution, TROPOMI NO_2 data with quality assurance value larger than 0.75 are annually averaged and gridded at 1 × 1 km^2 spatial resolution using an oversampling approach (i.e., gridding smaller than the original TROPOMI pixel size; Sun et al., 2018). For the emission estimation, we first apply the wind rotation technique as described by Fioletov et al. (2015) by rotating each pixel around the point source according to the wind direction so that all pixels

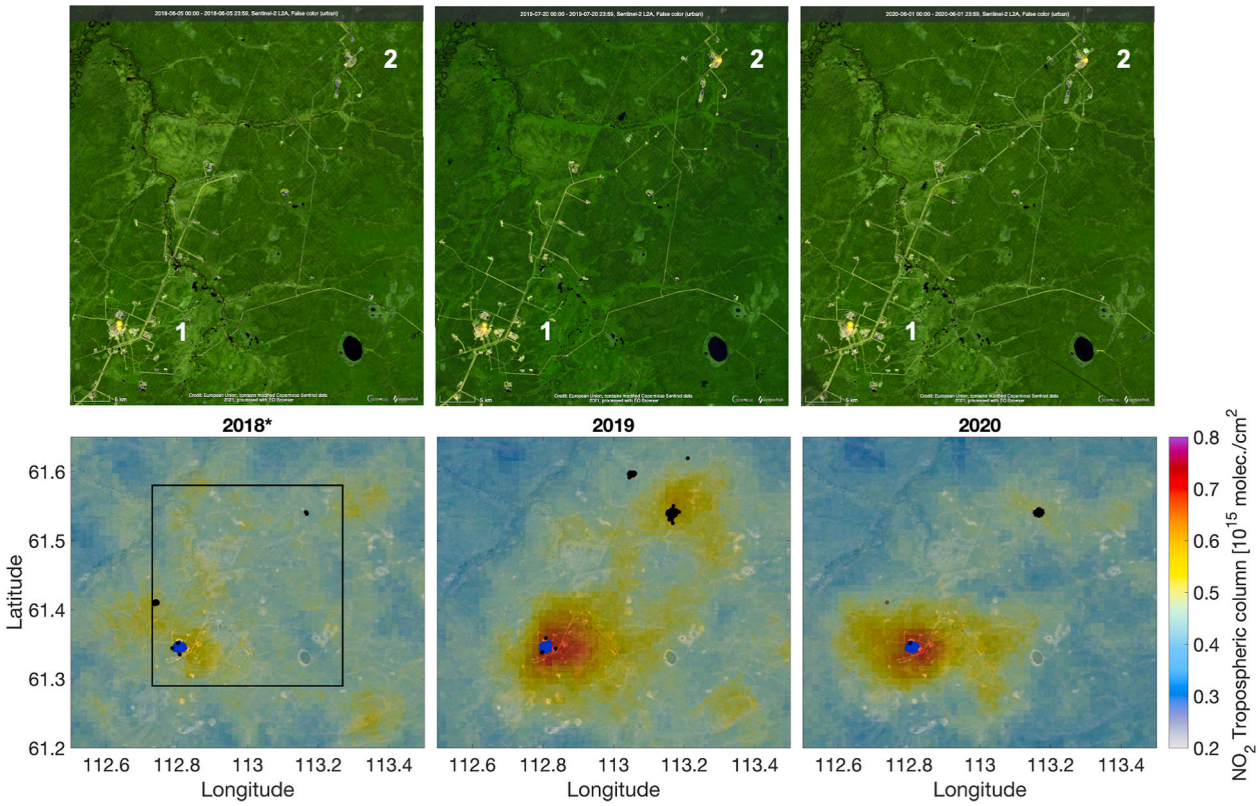

Fig. 2. Gas flaring signal detection over Tas-Yuryakh oil field. Upper panel: Sentinel 2 false color (urban) images on 5 June 2018, 20 July 2019 and 1 June 2020. Lower panel: Annual TROPOMI NO_2 average maps overlaid with VIIRS daytime active fire data. Data classified as fire type *presumed vegetation fire* and *other static land source* are shown as black and blue dots, respectively. Gray dots in 2020 correspond to NRT active fire data available without fire type information. The black rectangle in the bottom-left panel indicates the area covered by the Sentinel 2 images in the upper panels.

appear to have the same wind direction (from west to east). The wind information are derived from the ECMWF ERA5 data averaged over the vertical layers at 1000, 950 and 900 hPa pressure levels. For the estimation of the NO_x emission rate E, we first calculate the NO_2 line density by integrating the NO_2 annual tropospheric columns (after the rotation) over $\pm$50 km in the across-wind direction. We fit the NO_2 line densities with an exponentially-modified Gaussian function scaled by a multiplicative emission factor Q and an additive background parameter B (Beirle et al., 2011; Varon et al., 2018; Goldberg et al., 2019). The emission is $E = Q \times U$, where U is the median wind speed. Five parameters are estimated in the fitting procedure: the emission factor Q, the background B, the distance (along the upwind-downwind direction) of the linear density peak from the point source, the e-folding distance and the width of the Gaussian function σ. The posterior distribution of the fitted parameters is obtained using the Markov chain Monte Carlo (MCMC) sampling method (Laine, 2008; Haario et al., 2006). The estimate of the emission parameters are calculated as the mean values of the posterior distribution and the fitting uncertainties are obtained from the standard deviation of the posterior distribution around the estimate. The fitting error on the emission estimates here is only a few percents. In order to derive the NO_x emissions we assume a constant NO_x-to-NO_2 ratio of 1.32 as in Beirle et al. (2011).

The uncertainty on the emission rate E depends on different factors in addition to the model fitting error (e.g., Beirle et al., 2011; Fioletov et al., 2015; Goldberg et al., 2019): the error associated with TROPOMI tropospheric NO_2 column density (about 30%); the effect of the wind field information used in the rotation and in the emission calculation (about 20%); the uncertainty of the assumed NO_x-to-NO_2 ratio (10%); the choice of the integration area (less than 10%). The total uncertainties on the emission estimations are obtained using error propagation. We find that the first three factors contribute the most to the total uncertainty (about 40%). In addition, we note that the emission rates derived with this approach will only account for clear-sky conditions and will be biased toward spring-summer values. When only clear-sky pixels are taken into account, a negative bias is expected in the emission estimates, mostly because of the accelerated photo-chemistry. Also, changes in the emissions can affect the AMF (air mass factor) used in the NO_2 tropospheric column calculation. Emissions related to gas flaring are generally missing or underestimated in existing inventories. Lower emissions in the a priori information would lead to higher AMFs, resulting in smaller tropospheric columns and, in turn, smaller emission rates. Furthermore, since both sites are located at latitudes around 60°N, TROPOMI NO_2 observations are not available during winter over the facilities and the results will be further biased towards spring-summer conditions.

Finally, the volume of gas flared can be calculated by dividing the NO_x emission rates by a conversion factor of 1.56 $\pm$ 0.20 g/m^3, as described by Zhang et al. (2019).

2.3. TROPOMI CH_4 product and emission estimation method

We use column-averaged dry air mole fraction of methane (XCH_4) data retrieved from TROPOMI instrument to study the methane emissions over the oil fields. The retrieval algorithm simultaneously infers methane concentrations and physical scattering properties, using the spectra from the TROPOMI SWIR and NIR channels (Hu et al., 2016). The near-nadir spatial resolution of the infrared channels was 7 $\times$ 7 km^2 at the beginning of the mission and improved to 7 $\times$ 5.5 km^2, since 6 August 2019. The quality of TROPOMI CH_4 retrievals have been assessed against satellite-based GOSAT XCH_4 data (Hu et al., 2018) and ground-based TCCON observations (Lorente et al., 2021). Only XCH_4 measurements with quality assurance flag larger than 0.5 are used in the

analysis.

We assess the spatial distribution of methane over the oil fields by oversampling TROPOMI data over the period 30 April 2018–12 October 2020. We also estimate the methane emissions from individual TROPOMI orbits using the cross-sectional flux method as described by Varon et al. (2018, 2019). The method derives the methane emission rate from the cross-plume integral C computed over transects perpendicular to the wind direction at different distances from the source. The emission rate is given at each transect as $E = U \times C$, where U is the wind speed at the sources, which is estimated from the ECMWF ERA5 reanalysis data at vertical layers at 1000, 950 and 900 hPa pressure levels (as for NO_2). This average gives approximately the same value as $1.4 \times U_{10}$ (10 m wind) as found by Varon et al. (2018). The application of the method is illustrated in Sect. 3.2.

2.4. VIIRS active fire standard data and flared gas volume data

In order to identify the gas flares and their frequency, we use the 375 m active fire data from the Visible Infrared Imaging Radiometer Suite (VIIRS), operating on-board the joint NASA/NOAA Suomi-National Polar-orbiting Partnership (S-NPP) satellite since October 2011, as available from NASA's LANCE FIRMS archive. S-NPP VIIRS data are available twice a day at the equator (and possibly more at higher latitudes due to the overlap of different orbits) with overpass times approximately 13:30 p.m. (ascending node) and 1:30 a.m. (descending node). The S-NPP afternoon overpass is very close to the Sentinel-5P and the S-NPP VIIRS daytime observing conditions are similar to those from TROPOMI.

The VIIRS fire detection algorithm is based on the 375 m middle and thermal infrared imagery data (I-bands). In particular, the channel I4 (3.74 μm) is the primary driver of the fire detection algorithm (Schroeder et al., 2014). The algorithm builds on the MODIS (Moderate Resolution Imaging Spectroradiometer) active fire product using a contextual approach to detect both day and nighttime biomass burning and other thermal anomalies (Giglio et al., 2003). The product includes (among other variables) the time and coordinates of the fires as well as the corresponding fire radiative power (FRP, in MW). The standard quality active fire data also include information on the fire type: presumed vegetation fire, active volcano, other static land source and offshore. The fire pixels are classified as persistent static fire sources (i.e., no vegetation fires) for any grid cell in which fire pixels are detected on 50 or more unique calendar days per year (Giglio et al., 2006). These pixels mostly correspond to gas flares associated with oil and gas extraction. We used the annual active fire data product over Russia available in shapefile format from the FIRMS archive download: https://firms.modaps.eosdis.nasa.gov/download/.

In addition to the high resolution 375 m channels, VIIRS carries another set of multi-spectral channels (M-bands) at 750 m nominal resolution. Elvidge et al. (2013) developed a nightfire algorithm based primarily on the VIIRS 750 m short-wave infrared (1.61 μm) channel and Day-Night Band (DNB) data for the nighttime detection of gas flares. Based on this nightfire product, Elvidge et al. (2016) derived a global survey of natural gas flaring, including information on the volume of gas flared for 7467 individual sites. Annual global estimates until 2019 are available for download at https://eogdata.mines.edu/download_global_flare.html. The VIIRS volumes of gas flared for Tas-Yuryakh and Talakan are reported in Tables 1 and 2, respectively. These values will be compared to those obtained from the NO_x emissions from TROPOMI observations.

2.5. Sentinel 2 false color (urban) product

In order to confirm the location of the gas flares over the oil extraction facilities, we use false color images from Sentinel-2 as available from the Sentinel Hub EO Browser (https://apps.sentinel-hub.com/eo-browser).

Sentinel-2 is a wide-swath multi-spectral imaging mission that provides high-resolution (10 m, 20 m, and 60 m, depending on the wavelength) images for 13 spectral bands in the visible and infrared wavelengths. The mission is based on a constellation of two identical satellites, Sentinel-2A and Sentinel-2B, both flying on a sun-synchronous orbit. The Sentinel-2 mission is part of the Copernicus Land Monitoring Services and it is designed to monitor surface properties such as vegetation, soil and water cover. The images are available since March 2018 as 100×100 km^2 tiles, with maximum revisit time of 5 days (using both Sentinel-2A and 2B satellites).

The most common applications include land-cover mapping, land-use change detection as well as vegetation and forest fires monitoring. We use the false color (urban) product based on the composite of bands 12, 11 and 4. Vegetation is visible in shades of green, while constructed areas are represented by white or gray. Snow and ice appear as dark blue, and water as black or blue. Surfaces with elevated temperatures, such as forest fires and calderas of volcanoes, saturate the image in medium IR channels and are displayed in shades of red or yellow. To the same category belong also gas flares from oil extraction processes as those analysed in this work. Examples of such images are shown in Sect. 3.

2.6. NO_x and CH_4 emission inventories

We use the Community Emissions Data System (CEDS, McDuffie et al., 2020) NO_x emission inventory for comparison with the satellite-based emission estimations. Fig. S1 in the supplementary material shows the CEDS 2014 total NO_x emissions and those related to the energy sector only (left and right panel, respectively) over Tas-Yuryakh and Talakan, available on a $0.5^\circ \times 0.5^\circ$ grid. CEDS database reports about 0.05 mol/s over Talakan, with the largest fraction (over 90%) related to the energy sector. No clear enhancement in the emission patterns is visible over Tas-Yuryakh, for which the CEDS database reports about 0.003 mol/s.

We also used the Emissions Database for Global Atmospheric Research (EDGAR V5.0, Crippa et al., 2020), which is available on a $0.1^\circ \times 0.1^\circ$ grid. Fig. S2 in the supplementary material shows the EDGAR 2015 NO_x emissions from all sectors except transport. EDGAR inventory reports about 0.003 mol/s over Talakan (even though slightly displaced compared to the main oil pumping station) and about 0.01 mol/s near Tas-Yuryakh.

Fig. S3 in the supplement includes the CH_4 emissions from the fuel extraction sector (almost the only sector contributing to the total emission in the area) also available from the EDGAR v5.0 inventory. As further discussed in Sect. 3.2, we analyse the TROPOMI CH_4 observations only over Talakan, where the reported emission rate for 2015 is about 3 tons/h.

3. Results

3.1. Tas-Yuryakh

The location of the APG flares in Tas-Yuryakh can be detected as yellow-orange colors from the Sentinel 2 false color images (Fig. 2, top panels). The gas flaring signal over the main oil pumping station is visible for example on 5 June 2018, 20 July 2019 and 1 June 2020 (#1 in Fig. 2, top panels) and it is also regularly detected from every clear-sky Sentinel 2 image available since 1 March 2018. Correspondingly, a local enhancement is visible in the annual tropospheric NO_2 average maps over the same facility (bottom panels in Fig. 2). Here we note that the NO_2 annual map for 2018 includes TROPOMI observations only since April 15, so the mean fields are not completely comparable to the other years. On 20 July 2019 and 1 June 2020, another gas flaring signal is detected from the Sentinel 2 images over a second facility (#2 in Fig. 2, upper panels) located about 30 km north-east from the first. Correspondingly, another smaller NO_2 enhancement is visible in the 2019

average map (Fig. 2, bottom middle panel) over source #2. This second NO_2 enhancement is still visible in 2020 (Fig. 2, bottom right panel), but it is less evident than in 2019.

Fig. 2 (bottom panels) also shows the VIIRS active fire data for each year, classified as *presumed vegetation fires* or *other static land source* (black and blue dots, respectively). In order to represent observing conditions close to the afternoon orbit of S5P, only daytime active fire data are shown in Fig. 2. VIIRS detected persistent (561 daytime fire counts in 2019) flaring over the facility #1, co-located with the NO_2 enhancements. The fires are classified as static land source (blue dots in Fig. 2, bottom panels). Since 2019 VIIRS also detected flares over facility #2 (452 daytime fires in 2019 corresponding to the NO_2 enhancement), but the algorithm classifies them as presumed vegetation fires (black dots in Fig. 2, bottom middle panel), most probably because the source is new and not yet recognized as a static land source from VIIRS fire type algorithm. We note here that, the information on the fire type (included in the VIIRS standard product) is available only until 30 May 2020. After that date, we use Near Real Time (NRT) data (gray dots in Fig. 2, bottom right panel) that are available without fire type information. Therefore, there might be discrepancies in both fire counts and FRP values between 2020 and the previous years. The summary of the annual daytime and nighttime fire counts over Tas-Yuryakh facilities #1 and #2 is reported in Table 1.

Fig. 3 shows the time series of the daily mean FRP over Tas-Yuryakh oil field based on VIIRS 375m active fire data. We observe persistent flaring activity over facility #1 during the whole period of study (blue symbols in Fig. 3), while the fire detection over facility #2 starts toward the end of October 2018 and continues until the end of 2020 (red symbols in Fig. 3). This persistent detection indicates the occurrence of continuous production flaring at both sites, in which the gas stream is directed into a flare system because no re-utilization route is available.

Daytime active fire data (filled dots in Fig. 3) are limited between the end of March and the beginning of November, corresponding to similar observing conditions than TROPOMI on S5P, while nighttime data (crosses in Fig. 3) are available throughout the year. The daily mean FRP value is generally higher for facility #1 than for #2. For example, the daytime annual average FRP for 2019 according to VIIRS data is 19.8 MW for the first facility and 15.1 MW for the latter. This difference becomes ever larger in 2020, when the mean FRP in facility #1 is almost double than in facility #2 (Table 1).

Fig. 4 illustrates the NO_x emission estimation procedure over Tas-Yuryakh for 2019, based on the methodology described in Sect. 2.2. Fig. 4 (left panel) shows the 2019 annual mean of TROPOMI NO_2 tropospheric columns averaged using an oversampling approach on a 1 $\times$ 1 km^2 grid. Fig. 4 (middle panel) shows the NO_2 average map after rotating each pixels according to the wind direction around source #1 over an area with 200 km radius from the center. After the rotation, the NO_2 plume is distributed eastward from the source, as if the wind direction for all observations is out of the west. Applying the wind rotation better isolates the signal from the main source (#1 in Fig. 4) from the secondary enhancement (#2 in Fig. 4). The wind rotation redistributes the signal from the secondary source over a ring of 30 km radius around the main source, so that it is not detected anymore. In our case, we consider source #1 and #2 as a single source and we calculate the emission only rotating around source #1. The resulting emission rate will include a somewhat mixed contribution from both sources as explained by Fioletov et al. (2016).

Fig. 4 (right panel) shows the line density (blue dots) calculated from the integral in the across-wind direction of the NO_2 plume after the rotation (from Fig. 4, middle panel) and the exponentially-modified Gaussian model (black line) fitted to the data via MCMC approach. The resulting NO_x emission rate for 2019 (considering a NO_x-to-NO_2 ratio of 1.32) is 1.34 $\pm$ 0.46 mol/s. The NO_x emission estimates for 2018 to 2020 are reported in Table 1 together with their uncertainties. The emission rate for 2018 is calculated based on shorter time period including relatively more observations during summer. The resulting mean NO_2 fields have larger background noise and bias towards spring-summer conditions. Nevertheless, we find that the NO_x emissions for 2019 are about double than in 2018, consistent with the increase in the cumulative fire counts and FRP values over facility #1 and #2. This is also consistent with the 38% increase in oil production at the facility #1 and the beginning of extracting activities at the facility #2 with 854 Kton of crude oil production in 2019 (Table 1). In 2020, the NO_x emission slightly decreases, but the difference remains within the uncertainties.

Tas-Yuryakh emission source is missing from the CEMS database and underestimated in the EDGAR inventory (about 0.01 mol/s for 2015). This is possibly due to delayed or incomplete information on the contribution of the oil and gas sector in the inventories.

If we assume that the NO_x emissions are mostly due to APG flaring, the accompanying volume of gas flared can be calculated for each year using a conversion factor of 1.56 $\pm$ 0.20 g/m^3 as in Zhang et al. (2019) (Table 1). For example, in 2019 the volume is 1.25 $\pm$ 0.48 bcm, which is higher than the value reported for source #1 (0.75 $\pm$ 0.08 bcm) in the global survey of natural gas flaring based on VIIRS nightfire data (Elvidge et al., 2016). If we consider the sum of the volume of gas flared from facility #1 and #2 from the VIIRS survey (1.14 $\pm$ 0.11 bcm, Table 1), the resulting estimate becomes closer to the value obtained from the NO_x emissions. For 2018, the volumes of gas flared from TROPOMI (0.57 $\pm$ 0.22 bcm) and VIIRS (0.40 $\pm$ 0.04 bcm, cumulative for #1 and #2) also agree within the uncertainties and are about 50% smaller than for 2019. This is consistent with the increase in oil production and flaring activities observed in 2019. A similar increase can be seen in the annual environmental fees paid by oil companies (for the volume of gas flared that exceeds the allowed limit of 5%) to the Mirninsky district (where Tas-Yuryakh is located), which are about 40% lower in 2018 than in 2019 (31 million rubles in 2019 and 19 million

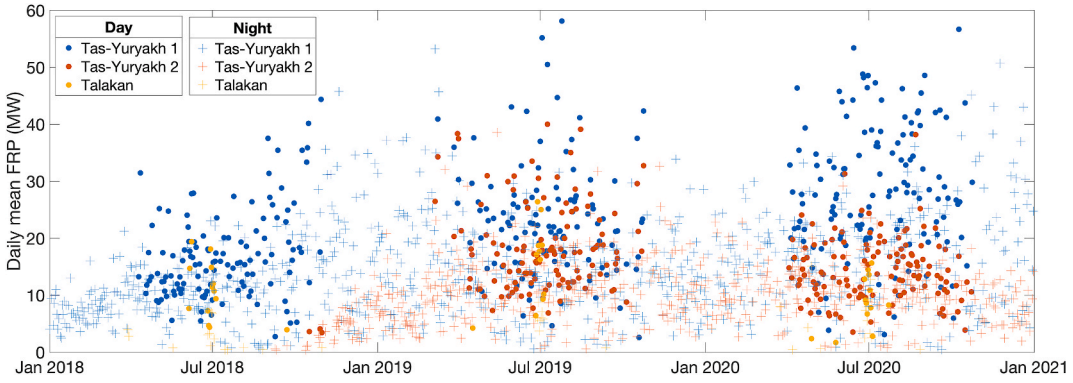

Fig. 3. VIIRS daily FRP (MW) averages over Tas-Yuryakh (blue and red symbols for facility #1 and #2, respectively) and Talakan (yellow symbols) oil extraction facilities. Dots and crosses indicate daytime and nighttime observations, respectively.

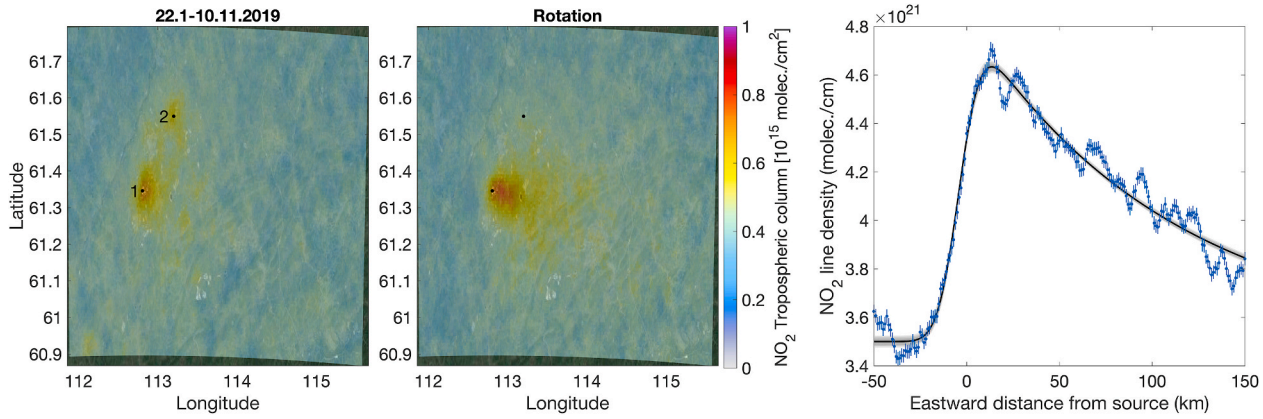

Fig. 4. Illustration of NO_x emission estimation procedure from TROPOMI observations. Left panel: 2019 average NO_2 tropospheric column. Middle panel: same as left panel but after rotation according to the wind direction. Right panel: NO_2 line density (blue dots) derived from the integral across plume from the middle panel and fitted exponentially-modified Gaussian model (black line).

rubles in 2018, Table 1).

3.2. Talakan

Fig. 5 (top panels) shows three Sentinel 2 false color images over the Talakan oil field on 27 June 2018, 5 July 2019 and 1 July 2020. A yellow-orange flaring signal is visible over the main oil pumping station in the bottom-right corner of the images. Differently from Tas-Yuryakh, such signal is only occasionally detected from Sentinel 2 images. VIIRS active fire data confirm the detection of the gas flares over the same oil pumping station in Talakan (blue dots in Fig. 5, lower panels) for all three years. VIIRS detected about ten times less flares in Talakan (53 daytime fires in 2019, Table 2) than in Tas-Yuryakh, indicating a much smaller gas flaring activity.

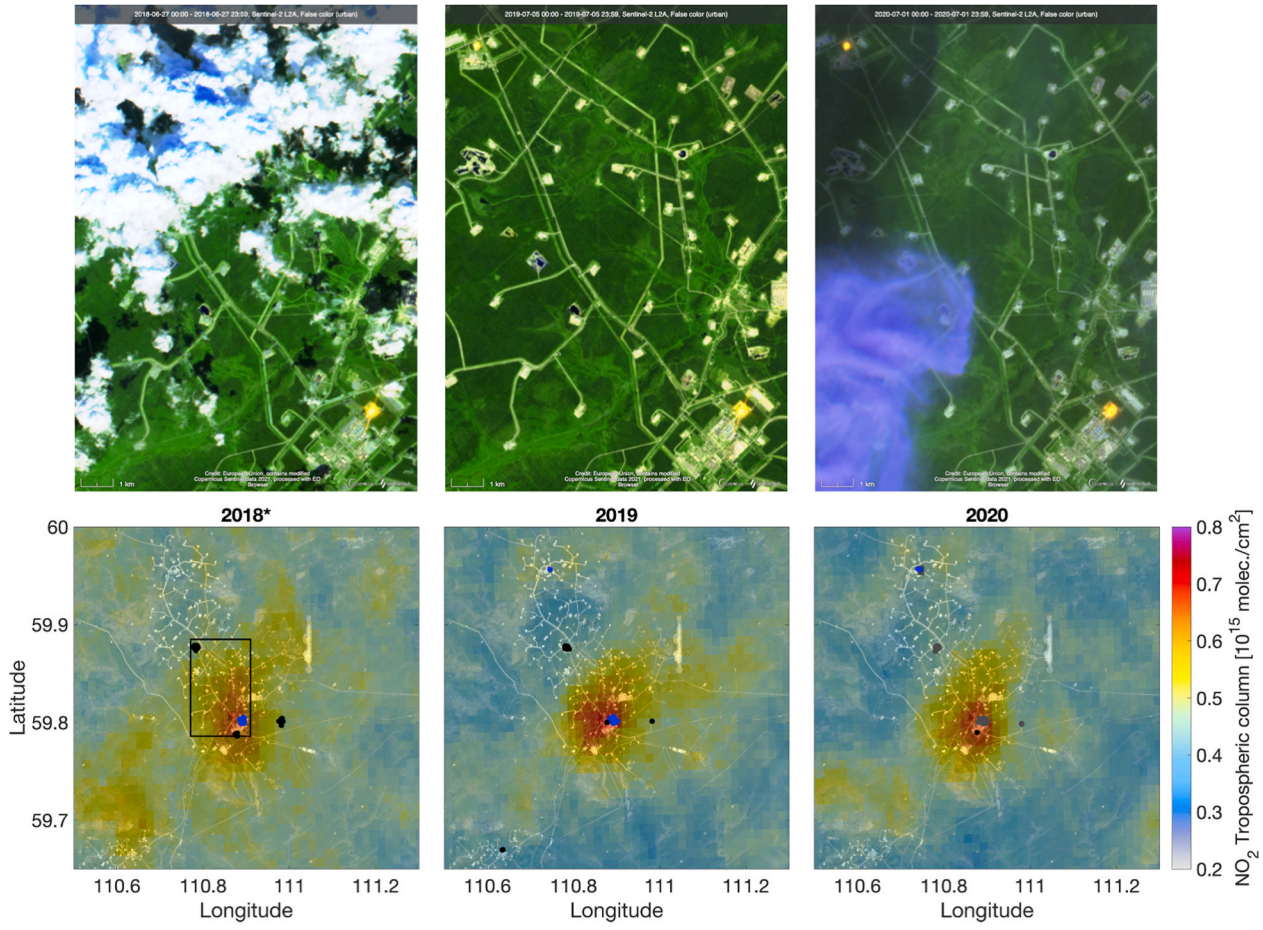

Fig. 5. Gas flaring signal detection over Talakan oil field. Upper panel: Sentinel 2 false color (urban) images on 27 June 2018, 5 July 2019 and 1 July 2020. Lower panel: Annual TROPOMI NO_2 average maps overlaid with VIIRS daytime active fire data. Data classified as fire type *presumed vegetation fire* and *other static land source* are shown as black and blue dots, respectively. Gray dots in the 2020 panel indicate VIIRS NRT data (available without fire type classification). The black rectangle in the bottom-left panel indicates the area covered by the Sentinel 2 images in the upper panels.

The time series of the FRPs over Talakan facilities (yellow symbols in Fig. 3) show that the flares are detected almost exclusively between the end of June and beginning of July of each year (as also shown by the Sentinel 2 images in Fig. 5, upper panels), suggesting that APG flaring only occurs during scheduled maintenance or safety procedures during summer. The daytime annual median FRP for 2019 is 10.7 MW, which is almost half than for Tas-Yuryakh source #1.

The TROPOMI tropospheric NO_2 average maps show local NO_2 enhancements, corresponding to the location of the flares, for all three years (Fig. 5, bottom panels). Occasionally a flaring signal is observed over a second site a few kilometers north-west from the main source from both Sentinel 2 images and VIIRS data, but no clear enhancement is visible from the NO_2 average maps (Fig. 5).

We calculated the NO_x emissions over Talakan from TROPOMI observations as described in Sect. 2.2 and illustrated in Fig. 4 for Tas-Yuryakh. The results are summarized in Table 2. The NO_x emissions (about 0.6 mol/s) over Talakan remain approximately constant (within the uncertainties) from 2018 to 2020. This value is similar to the NO_x emissions obtained in Tas-Yuryakh for 2018, before the increase in oil production and flaring activity in 2019. These NO_x emissions are higher than those reported in the EDGAR and CEDS inventories near Talakan (0.003 and 0.05 mol/s, respectively), suggesting again missing information in both databases. The corresponding volume of APG flared, assuming that all NO_x emissions are related to gas flaring, would be about 0.5 bcm, which is one order of magnitude larger than the value reported in the VIIRS gas flaring survey (about 0.025 bcm, Table 2). This suggests that a substantial fraction of the estimated emissions might be related to other combustion processes in the oil production, such as heating and power generation. The energy supply of oil production and oil-pump station is provided by the 144 MW Talakan Gas-Tourbine Power Plant (GTPP) and 12.7 MW Gas Generation Station, both powered by APG. Talakan deposit industrial facilities heating is provided by the Talakan GTPP heat utilizers and 15 boiler houses with a total capacity of 82.3 Gcal/h.

On the other hand, since the annual average NO_2 fields at middle-high latitudes are biased towards summer days and APG flaring occurs only during summer in Talakan, the annual NO_x emissions might be overestimated. Zhang et al. (2019) also found that their estimate of volume of gas flared based on NO_x emissions are larger than VIIRS-based estimates in Mexico's offshore oil field. At the same time, under the assumption of constant emissions throughout the year, the accelerated photo-chemistry during summertime would lead to an underestimation of the annual emissions. Finally, the VIIRS-based survey depend on the accuracy of national bottom-up emission information, which might be incomplete.

Table 2 shows that the oil production is similar during different years, as for the NO_x emissions. The oil production in 2019 in Talakan is two times larger than in Tas-Yuryakh, while the NO_x emissions are about two times smaller. This confirms that gas flaring contributes substantially to the polluting emissions in Tas-Yuryakh, where persistent flaring occurs throughout the year, while the emission is much smaller in Talakan, where flaring is only employed for a couple of weeks each year. Consistently, the amount of environmental fees for the APG flaring paid to the Lensky district (where Talakan oil pumping station is located) is about three orders of magnitude smaller than for Mirninsky district.

Fig. 6 shows the TROPOMI average CH_4 anomalies (differences from background value) over Talakan, gridded at 1×1 km^2 using oversampling over the period 30 April 2018–10 December 2020. The background is calculated from the mean of the XCH_4 values smaller than 1840 ppb over the area shown in Fig. 6. We observe a XCH_4 anomaly up to 30 ppb near Talakan facilities, possibly related to venting, leakage or outflow from the flaring itself. We note that many of the TROPOMI pixels over the flaring site (black diamond in Fig. 6) are actually excluded from the average by the TROPOMI CH_4 quality flag. Fig. S4 in the supplementary material shows that the number of valid observations over the flaring site is about half compared to the surroundings. This

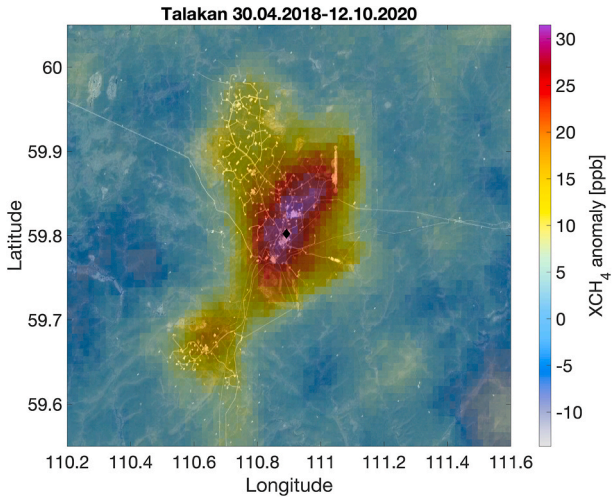

Fig. 6. TROPOMI average XCH_4 anomaly over Talakan during the period 30 April 2018–10 December 2020. The black diamond indicates the location of the main flaring site.

suggests that the quality flag rejects the scenes corresponding to flares, possibly due to the large aerosol load or otherwise unsuccessful retrieval. This introduces a larger statistical error in the calculation of the mean CH_4 fields. Nevertheless, the CH_4 enhancement is clearly visible near Talakan, including smaller enhancements in the south-west and north-west branches of the oil field.

Another CH_4 enhancement is visible over the Verhnechonskoye oil and gas field located about 90 km west from Talakan, in the Kataganskiy district of Irkutsk Oblast (Fig. S5 in the supplement). According to VIIRS gas flaring survey data, in Verhnechonskoye the volume of APG flared (0.15 bcm in 2019) is almost ten times larger than in Talakan. This suggests more frequent gas flaring activities in Verhnechonskoye. This would explain the anomalously low XCH_4 value over Verhnechonskoye flaring site (black square in Fig. S5), which comes from a very small amount of valid TROPOMI observations just over the site. On the other hand, on the eastern part of the oil field, the XCH_4 anomaly values are 20–30 ppb. A NO_2 enhancement up to about 0.6×10^{15} molec./cm^2 is also visible over Verhnechonskoye (not shown).

In order to estimate the CH_4 emissions we applied the cross-sectional flux method to TROPOMI CH_4 retrievals from individual plumes as described by Varon et al. (2018, 2019). Fig. 7 illustrates an example of the calculation of the CH_4 emission on 11 August 2020. The emission E is derived from the integrals C across-wind over several transects (white dotted lines in Fig. 7), located at regular distance downwind from the source. The numbers near each transect indicate the value (in tons/h) of the emission $E = U \times C$, where U is the mean wind speed near the source. We note that there are possibly multiple CH_4 sources near Talakan oil pumping station, as also visible from Fig. 6, and we consider all the transects over the observed plume (CH_4 enhancement), independently from the location of the main oil pumping station. The background is defined from the average over the area upwind from the source (pink dots in Fig. 7). On 11 August 2020 we obtain emission values in the range 21–35 tons/h (average 28 tons/h).

We identified a few CH_4 plumes near Talakan suitable for the emission calculation, but the definition of the integration and background areas is challenging and somewhat subjective, due to the large background noise. Fig. S6 in the supplement shows another example (on 23 September 2018) for which it was possible to clearly identify the CH_4 plume from the background and to carry on the emission estimation. On 23 September 2018 we obtain emission rates in the range 37–85 tons/h (average 63 tons/h). These two cases were selected as the most reliable scenes (with a clear separation between the CH_4 plume and the background) for the emission estimation among less than 10 potential scenes

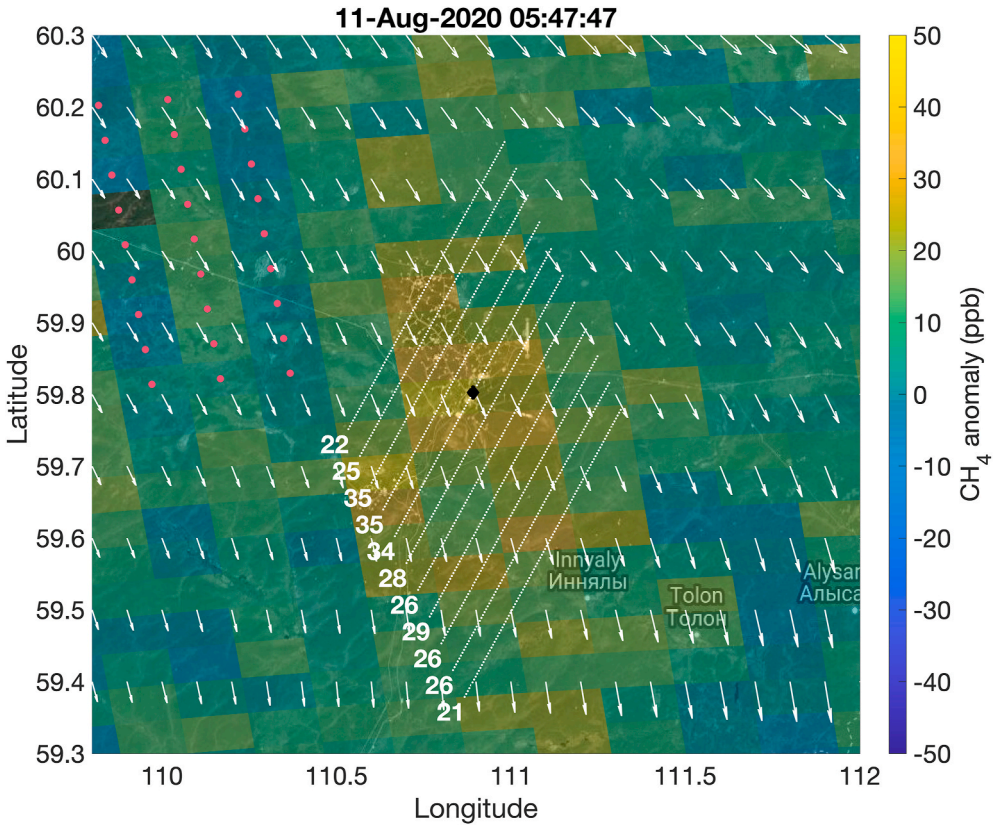

Fig. 7. TROPOMI XCH_4 anomaly over Talakan on 11 August 2020. The white dotted lines indicate the transects where the integral across-wind is calculated over the CH_4 plume. The white arrows indicated the ERA5 wind information averaged from 1000, 950 and 900 hPa pressure levels. The background area is calculated from the pixels marked by the pink dots. The black diamond indicates the location of the main flaring site.

with a sufficient amount of valid retrievals near Talakan facilities. Overall, the estimated emission values are considerably larger than those reported in the EDGAR inventory for 2015 (about 3 tons/h), but they are similar to the values reported by Varon et al. (2019) in Korpezhe oil and gas field (Turkmenistan) or by Conley et al. (2016) from the Aliso Canyon (Los Angeles, California) gas storage blowout.

We attempted a similar approach to identify CH_4 enhancements in Tas-Yuryakh, but the persistent occurrence of flares yield all CH_4 retrievals over the facilities to be rejected by the quality assurance flag or to have anomalously low XCH_4 values (as in Verhnechonskoye). This underlines the limitations in using satellite-based passive observations to monitor methane emissions over oil fields where gas flaring also occurs, especially at high latitudes where limited sunlight in winter and frequent cloudy conditions reduce the amount of observations available for such analysis.

4. Summary and discussion

We analysed the NO_x and CH_4 emissions over the Tas-Yuryakh and Talakan oil fields in Sakha Republic, Russia, by using satellite observations from multiple platforms. We detected persistent APG flaring in Tas-Yuryakh using Sentinel 2 and VIIRS data and corresponding local enhancements in the TROPOMI NO_2 mean fields. In Talakan we detected APG flares only between the end of June and beginning of July of each year. While having about three times larger oil production, the NO_x emissions estimated from TROPOMI observations in Talakan are about half of those in Tas-Yuryakh for 2019. The amount of flares detected in Talakan is about ten times smaller than in Tas-Yuryakh. Overall, the changes in the annual amount and intensity of the flares appear to track those of the collocated NO_x emissions, which supports the assumption that the emissions are linked to gas flaring activities.

The analysis of the TROPOMI XCH_4 mean fields enabled the accurate identification of the XCH_4 spatial distribution around the source. Due to the limited amount of valid observations, the CH_4 emission estimation over oil fields can be challenging, especially at relatively high latitudes, with frequent cloudy conditions and low solar zenith angles during winter. Nevertheless, we estimated CH_4 emission rates up to about 63 tons/h in Talakan based on TROPOMI observations.

The amount of budget income from APG flaring fees paid by companies is about three orders of magnitude larger in the Mirninsky district (where Tas-Yuryakh is located), compared to the Lensky district (including Talakan oil field). Surgutneftegas, the company operating in Talakan, declares to utilize about 99% of the APG for power generation and other re-utilization procedures, and therefore gas flaring is limited to scheduled maintenance and safety operations, which is consistent with our results (https://www.surgutneftegas.ru/upload/iblock/06c/ECO/2019/eng.pdf). On the other hand, both companies operating in Tas-Yuryakh, Rosneft and RNG (facility #1 and #2, respectively), appear to use routine or production flaring for disposing the APG during the crude oil extraction. RNG operates Caterpillar gas engines and utilizes some of the extracted APG for power production (http://rngoil.ru/wp-content/uploads/rng-sustainable-report-2019-ru-south-west.pdf), but routine gas flaring is still observed at the facility #2. RNG also declares an increase in gas re-utilization from 2019 to 2020 due to the plans to launch the second and third stages of the power generation and to bring the total capacity from 5 MW to 12 MW. Correspondingly, we observe a reduction in the average FRP and NO_2 tropospheric columns near the facility #2 in 2020, as compared to 2019. Recently, the company declared the start of a project for the reinjection of the APG into the oil reservoir, which should reduce gas flaring significantly (http://rngoil.ru/news/rng-purchased-gas-reinjection-equipment/).

Both the NO_x and CH_4 emissions estimated from TROPOMI

observations are higher than the existing inventories. Bottom-up emission inventories for the oil and gas industry are often incomplete due to challenges in quantifying the emissions from APG flaring or to incomplete reporting by individual companies. Satellite-based observations are therefore very useful to provide more complete and timely emission estimates. In particular, improved knowledge about the NO_x and CH_4 emissions from the oil and gas industry is needed to evaluate the effects of the replacement of coal-based energy systems on air quality and climate. The results also help evaluating the commitment of oil companies to reach the goal set by the Russian government to reduce the fraction of APG flaring to 5%.

Future plans to exploit new oil reserves in eastern Russia and Arctic, call for continuous monitoring of air polluting emissions over oil fields. Apart from adjusting the coefficient for excess APG flaring as a stimulating/tightening measure, with the plan of the Russian Federation to develop green financing (https://veb.ru/files/?file=70a471b4aec7d53a92c94edba906e9a9.pdf), the environment protection policies should focus on the development of APG utilization investment and technologies to make APG a valuable and efficient energy resource, especially in energy-isolated regions. For example, the Russian Federation plans to develop oil and gas industry in the Arctic (where the excessive APG flaring coefficient 0.25 is applied on the environmental fees for the Arctic shelf raw hydrocarbons deposits development) should be accompanied with green APG utilization support.

Since satellite observations offer global coverage, the approach presented here can be applied elsewhere to provide timely estimates of polluting emissions associated with APG flaring and oil production in general, especially where no other monitoring system is in place, and thereby support environmental monitoring by governmental authorities, nature protection organisations, and the oil industry itself.

5. Data availability

TROPOMI NO_2 and CH_4 data are available from the Sentinel-5P Pre-Operations Data Hub (https://s5phub.copernicus.eu/) and also at NASA's GES DISC (https://disc.gsfc.nasa.gov/). NASA VIIRS Active Fire data (SHP format) data set is provided by LANCE FIRMS and it is available online at: https://earthdata.nasa.gov/active-fire-data. The volumes of gas flared derived from VIIRS nightfire are available at https://eogdata.mines.edu/download_global_flare.html. Sentinel 2 imagery is available from the EO Browser website https://apps.sentinel-hub.com/eo-browser. EDGAR emission inventories are available at https://edgar.jrc.ec.europa.eu/. CEDS emission inventories are available at http://www.globalchange.umd.edu/ceds/.

Oil production data by companies are available in the State Annual Reports on the State of the Environment in the Sakha Republic (Yakutia) at https://minpriroda.sakha.gov.ru/gosdoklady-o-sostojanii-okruzhajuschej-sredy. Oil production data by the districts are available from Sakha (Yakutia) statistics on demand and the Ministry of Industries and Geology of Sakha Republic (Yakutia) at https://minprom.sakha.gov.ru/neftegazovaja-promyshlennost, and the official reports of the municipal districts at https://mr-lenskij.sakha.gov.ru/sotsialno-ekonomicheskoe-polozhenie-lenskogo-rajona. District budget data are available in the Annual and Monthly reports on the Municipal Budgets implementation at https://minfin.sakha.gov.ru/otchetnost. The scheme and program for the development of the electric power industry of the Republic of Sakha (Yakutia) for 2020–2024 is available at https://docs.cntd.ru/document/570789897.

CRediT authorship contribution statement

Iolanda Ialongo: Conceptualization, Methodology, Software, Formal analysis, Writing – original draft, Writing – review & editing, Funding acquisition. **Nadezhda Stepanova:** Formal analysis, Investigation, Writing – review & editing. **Janne Hakkarainen:** Formal analysis, Software, Writing – review & editing, Funding acquisition. **Henrik Virta:** Formal analysis, Software, Writing – review & editing. **Daria Gritsenko:** Funding acquisition, Writing – review & editing.

Declaration of competing interest

The authors declare that they have no known competing financial interests or personal relationships that could have appeared to influence the work reported in this paper.

Acknowledgement

This study was funded by the European Space Agency via DACES project. We also acknowledge the funding from the Academy of Finland (projects 324499, 337552, 336798 and 331829) and the European Union's H2020 projects e-shape (grant no. 820852) and CoCO2 (grant no. 958927).

Appendix A. Supplementary data

Supplementary data to this article can be found online at https://doi.org/10.1016/j.aeaoa.2021.100114.

References

van der A, R.J., de Laat, A.T.J., Ding, J., Eskes, H.J., 2020. Connecting the dots: NO_x emissions along a West Siberian natural gas pipeline. NPJ Clim. Atmos. Sci. 3, 16. https://doi.org/10.1038/s41612-020-0119-z.

Beirle, S., Boersma, K.F., Platt, U., Lawrence, M.G., Wagner, T., 2011. Megacity emissions and lifetimes of nitrogen oxides probed from space. Science 333, 1737–1739. https://doi.org/10.1126/science.1207824.

Conley, S., Franco, G., Faloona, I., Blake, D.R., Peischl, J., Ryerson, T.B., 2016. Methane emissions from the 2015 Aliso Canyon blowout in Los Angeles, CA. Science 351, 1317–1320. https://doi.org/10.1126/science.aaf2348.

Crippa, M., Solazzo, E., Huang, G., Guizzardi, D., Koffi, E., Muntean, M., Schieberle, C., Friedrich, R., Janssens-Maenhout, G., 2020. High resolution temporal profiles in the Emissions Database for Global Atmospheric Research. Sci. Data 7, 121. https://doi.org/10.1038/s41597-020-0462-2.

Crosman, E., 2021. Meteorological drivers of Permian Basin methane anomalies derived from TROPOMI. Rem. Sens. 13 https://doi.org/10.3390/rs13050896.

Dix, B., de Bruin, J., Roosenbrand, E., Vlemmix, T., Francoeur, C., Gorchov-Negron, A., McDonald, B., Zhizhin, M., Elvidge, C., Veefkind, P., Levelt, P., de Gouw, J., 2020. Nitrogen oxide emissions from U.S. oil and gas production: recent trends and source attribution. Geophys. Res. Lett. 47, e2019GL085866 https://doi.org/10.1029/2019GL085866.

Elvidge, C.D., Zhizhin, M., Hsu, F.C., Baugh, K.E., 2013. VIIRS Nightfire: satellite pyrometry at night. Rem. Sens. 5, 4423–4449. https://doi.org/10.3390/rs5094423.

Elvidge, C.D., Zhizhin, M., Baugh, K., Hsu, F.C., Ghosh, T., 2016. Methods for global survey of natural gas flaring from Visible Infrared Imaging Radiometer Suite data. Energies 9. https://doi.org/10.3390/en9010014.

Fioletov, V.E., McLinden, C.A., Krotkov, N., Li, C., 2015. Lifetimes and emissions of SO_2 from point sources estimated from OMI. Geophys. Res. Lett. 42, 1969–1976. https://doi.org/10.1002/2015GL063148.

Fioletov, V.E., McLinden, C.A., Krotkov, N., Li, C., Joiner, J., Theys, N., Carn, S., Moran, M.D., 2016. A global catalogue of large SO_2 sources and emissions derived from the Ozone Monitoring Instrument. Atmos. Chem. Phys. 16, 11497–11519. https://doi.org/10.5194/acp-16-11497-2016.

van Geffen, J.H.G.M., Eskes, H.J., Boersma, K.F., Maasakkers, J.D., Veefkind, J.P., 2019. TROPOMI ATBD of the Total and Tropospheric NO_2 Data Products. Technical Report. https://sentinel.esa.int/documents/247904/2476257/Sentinel-5P-TROPOMI-ATBD-NO2-data-products.

Giglio, L., Descloitres, J., Justice, C.O., Kaufman, Y.J., 2003. An enhanced contextual fire detection algorithm for MODIS. Rem. Sens. Environ. 87, 273–282. https://doi.org/10.1016/S0034-4257(03)00184-6.

Giglio, L., Csiszar, I., Justice, C.O., 2006. Global distribution and seasonality of active fires as observed with the Terra and Aqua moderate resolution imaging spectroradiometer (MODIS) sensors. J. Geophys. Res.: Biogeosciences 111. https://doi.org/10.1029/2005JG000142.

Goldberg, D.L., Lu, Z., Streets, D.G., de Foy, B., Griffin, D., McLinden, C.A., Lamsal, L.N., Krotkov, N.A., Eskes, H., 2019. Enhanced capabilities of TROPOMI NO_2: estimating NO_x from North American cities and power plants. Environ. Sci. Technol. 53, 12594–12601. https://doi.org/10.1021/acs.est.9b04488.

de Gouw, J.A., Veefkind, J.P., Roosenbrand, E., Dix, B., Lin, J.C., Landgraf, J., Levelt, P.F., 2020. Daily satellite observations of methane from oil and gas production regions in the United States. Sci. Rep. 10, 1379. https://doi.org/10.1038/s41598-020-57678-4.

Griffin, D., Zhao, X., McLinden, C.A., Boersma, F., Bourassa, A., Dammers, E., Degenstein, D., Eskes, H., Fehr, L., Fioletov, V., Hayden, K., Kharol, S.K., Li, S.M., Makar, P., Martin, R.V., Mihele, C., Mittermeier, R.L., Krotkov, N., Sneep, M., Lamsal, L.N., Linden, M.t., Geffen, J.v., Veefkind, P., Wolde, M., 2019. High-

resolution mapping of nitrogen dioxide with TROPOMI: first results and validation over the Canadian oil sands. Geophys. Res. Lett. 46, 1049–1060. https://doi.org/10.1029/2018GL081095.

Haario, H., Laine, M., Mira, A., Saksman, E., 2006. DRAM: efficient adaptive MCMC. Stat. Comput. 16, 339–354. https://doi.org/10.1007/s11222-006-9438-0.

Hu, H., Hasekamp, O., Butz, A., Galli, A., Landgraf, J., Aan de Brugh, J., Borsdorff, T., Scheepmaker, R., Aben, I., 2016. The operational methane retrieval algorithm for TROPOMI. Atmos. Meas. Tech. 9, 5423–5440. https://doi.org/10.5194/amt-9-5423-2016.

Hu, H., Landgraf, J., Detmers, R., Borsdorff, T., Aan de Brugh, J., Aben, I., Butz, A., Hasekamp, O., 2018. Toward global mapping of methane with TROPOMI: first results and intersatellite comparison to GOSAT. Geophys. Res. Lett. 45, 3682–3689. https://doi.org/10.1002/2018GL077259.

Ialongo, I., Virta, H., Eskes, H., Hovila, J., Douros, J., 2020. Comparison of TROPOMI/Sentinel-5 Precursor NO_2 observations with ground-based measurements in Helsinki. Atmos. Meas. Tech. 13, 205–218. https://doi.org/10.5194/amt-13-205-2020.

IPCC, 2014. In: Pachauri, R.K., Meyer, L.A. (Eds.), Climate Change 2014: Synthesis Report. Contribution of Working Groups I, II and III to the Fifth Assessment Report of the Intergovernmental Panel on Climate Change [Core Writing Team. IPCC, Geneva, Switzerland, p. 151. https://www.ipcc.ch/site/assets/uploads/2018/02/SYR_AR5_FINAL_full.pdf.

Laine, M., 2008. Adaptive MCMC Methods with Applications in Environmental and Geophysical Models. Finnish Meteorological Institute Contributions, 69. http://hdl.handle.net/10138/1149. ISBN:978-951-697-662-7.

Li, C., Hsu, N.C., Sayer, A.M., Krotkov, N.A., Fu, J.S., Lamsal, L.N., Lee, J., Tsay, S.C., 2016. Satellite observation of pollutant emissions from gas flaring activities near the Arctic. Atmos. Environ. 133, 1–11. https://doi.org/10.1016/j.atmosenv.2016.03.019.

Lorente, A., Borsdorff, T., Butz, A., Hasekamp, O., aan de Brugh, J., Schneider, A., Wu, L., Hase, F., Kivi, R., Wunch, D., Pollard, D.F., Shiomi, K., Deutscher, N.M., Velazco, V. A., Roehl, C.M., Wennberg, P.O., Warneke, T., Landgraf, J., 2021. Methane retrieved from TROPOMI: improvement of the data product and validation of the first 2 years of measurements. Atmos. Meas. Tech. 14, 665–684. https://doi.org/10.5194/amt-14-665-2021.

McDuffie, E.E., Smith, S.J., O'Rourke, P., Tibrewal, K., Venkataraman, C., Marais, E.A., Zheng, B., Crippa, M., Brauer, M., Martin, R.V., 2020. A global anthropogenic emission inventory of atmospheric pollutants from sector- and fuel-specific sources (1970–2017): an application of the Community Emissions Data System (CEDS). Earth Syst. Sci. Data 12, 3413–3442. https://doi.org/10.5194/essd-12-3413-2020.

McLinden, C.A., Fioletov, V., Boersma, K.F., Kharol, S.K., Krotkov, N., Lamsal, L., Makar, P.A., Martin, R.V., Veefkind, J.P., Yang, K., 2014. Improved satellite retrievals of NO_2 and SO_2 over the Canadian oil sands and comparisons with surface measurements. Atmos. Chem. Phys. 14, 3637–3656. https://doi.org/10.5194/acp-14-3637-2014.

Russian Federation, 2020. 2020 National Inventory Report (NIR). https://unfccc.int/documents/226417.

Rustamov, Z., Bryukhova, K., 2019. The problem of associated oil gas utilization, analysis and current status. Perm Natl. Res. Polytech. Univ. Aero. Eng. Bull. 102–109. https://doi.org/10.15593/2224-9982/2019.58.08.

Schneising, O., Buchwitz, M., Reuter, M., Vanselow, S., Bovensmann, H., Burrows, J.P., 2020. Remote sensing of methane leakage from natural gas and petroleum systems revisited. Atmos. Chem. Phys. 20, 9169–9182. https://doi.org/10.5194/acp-20-9169-2020.

Schroeder, W., Oliva, P., Giglio, L., Csiszar, I.A., 2014. The new VIIRS 375m active fire detection data product: algorithm description and initial assessment. Rem. Sens. Environ. 143, 85–96. https://doi.org/10.1016/j.rse.2013.12.008.

Sun, K., Zhu, L., Cady-Pereira, K., Chan Miller, C., Chance, K., Clarisse, L., Coheur, P.F., González Abad, G., Huang, G., Liu, X., Van Damme, M., Yang, K., Zondlo, M., 2018. A physics-based approach to oversample multi-satellite, multispecies observations to a common grid. Atmos. Meas. Tech. 11, 6679–6701. https://doi.org/10.5194/amt-11-6679-2018.

Varon, D.J., Jacob, D.J., McKeever, J., Jervis, D., Durak, B.O.A., Xia, Y., Huang, Y., 2018. Quantifying methane point sources from fine-scale satellite observations of atmospheric methane plumes. Atmos. Meas. Tech. 11, 5673–5686. https://doi.org/10.5194/amt-11-5673-2018.

Varon, D., McKeever, J., Jervis, D., Maasakkers, J.D., Pandey, S., Houweling, S., Aben, I., Scarpelli, T., Jacob, D., 2019. Satellite discovery of anomalously large methane point sources from oil/gas production. Geophys. Res. Lett. 46, 13507–13516. https://doi.org/10.1029/2019GL083798.

Veefkind, J., Aben, I., McMullan, K., Förster, H., de Vries, J., Otter, G., Claas, J., Eskes, H., de Haan, J., Kleipool, Q., van Weele, M., Hasekamp, O., Hoogeveen, R., Landgraf, J., Snel, R., Tol, P., Ingmann, P., Voors, R., Kruizinga, B., Vink, R., Visser, H., Levelt, P., 2012. TROPOMI on the ESA Sentinel-5 Precursor: a GMES mission for global observations of the atmospheric composition for climate, air quality and ozone layer applications. Rem. Sens. Environ. 120, 70–83. https://doi.org/10.1016/j.rse.2011.09.027 (The Sentinel Missions - New Opportunities for Science).

Vorobev, A., Shchesnyak, E., 2019. Associated petroleum gas flaring: the problem and possible solution. In: Glagolev, S. (Ed.), 14th International Congress for Applied Mineralogy (ICAM2019). Springer International Publishing, Cham, pp. 227–230. https://doi.org/10.1007/978-3-030-22974-0_55.

Zhang, Y., Gautam, R., Zavala-Araiza, D., Jacob, D.J., Zhang, R., Zhu, L., Sheng, J.X., Scarpelli, T., 2019. Satellite-observed changes in Mexico's offshore gas flaring activity linked to oil/gas regulations. Geophys. Res. Lett. 46, 1879–1888. https://doi.org/10.1029/2018GL081145.

Zhang, Y., Gautam, R., Pandey, S., Omara, M., Maasakkers, J.D., Sadavarte, P., Lyon, D., Nesser, H., Sulprizio, M.P., Varon, D.J., Zhang, R., Houweling, S., Zavala-Araiza, D., Alvarez, R.A., Lorente, A., Hamburg, S.P., Aben, I., Jacob, D.J., 2020. Quantifying methane emissions from the largest oil-producing basin in the United States from space. Sci. Adv. 6 https://doi.org/10.1126/sciadv.aaz51200.